Desalination 401 (2017) 120–133

Contents lists available at ScienceDirect

Desalination

journal homepage: www.elsevier.com/locate/desal

Evaluation of osmotic energy extraction via FEM modeling and exploration of PRO operational parameter space

Abraham Sagiv [a], Wenyan Xu [c], Panagiotis D. Christofides [b], Yoram Cohen [b,*], Raphael Semiat [a,*]

[a] Wolfson Faculty of Chemical Engineering, Technion – Israel Institute of Technology, Technion City, Haifa 32000, Israel
[b] Department of Chemical and Biomolecular Engineering, University of California, Los Angeles, CA, USA
[c] School of Life and Environment Sciences, Shanghai Normal University, Shanghai 200234, China

ARTICLE INFO

Article history:
Received 18 May 2016
Received in revised form 14 September 2016
Accepted 17 September 2016
Available online 28 September 2016

Keywords:
Pressure retarded osmosis
Osmotic energy
Finite element PRO model
PRO process analysis
Power density

ABSTRACT

Power generation via pressure retarded osmosis (PRO) was explored based on a detailed two dimensional finite-element (2-D-FEM) PRO model. Using the numerical model, an approach is presented for determining the draw and feed crossflow velocities for maximizing peak power generation. The dependence of PRO power generation on channel dimensions, membrane transport parameters were then evaluated, followed by assessing the impact of frictional pressure losses and pumping and energy recovery device (ERD) efficiencies. Illustrative test cases are presented for three different draw/feed streams representing seawater/brackish water (SW/BW), seawater RO-brine/brackish water (SWB/BW), and Dead Sea water/Seawater RO-brine (DSW/SWB). The maximum peak power density attainable via PRO was for DSW/SWB (35.3 W/m^2), followed by SWB/BW (7.29 W/m^2) and SW/BW (3.53 W/m^2) for the case of ideal pumps and ERD. For the optimistic Power generation from DSW/SWB PRO, high efficiency pumps (98%) and ERD (96%) would be required for peak power density to approach ~12 W/m^2 and 1.6 W/m^2 for the cases of DSW/SWB and SWB/BW, respectively, while net positive power generation is not expected for SW/BW. Higher permeability membranes could provide somewhat increased PRO performance; however, frictional pressure loses and less than ideal pumps and ERDs present a barrier for PRO as a viable approach for energy generation.

1. Introduction

In recent years there has been a renewed interest in energy production through the use of salinity (or osmotic pressure) gradients via the process of pressure retarded osmosis (PRO). The approach relies on having high and low salinity solutions flowing in two channels separated by a semi-permeable membrane that allows water permeation (from the low to high salinity solution) while rejecting the passage of salt ions [1,2]. It has been proposed that the extraction of osmotic energy may be practically (or commercially) feasible when streams of high salinity difference are readily available, as for example at the location where a river flows into the sea [2]. Another example of a location often touted as promising for PRO energy production is the meeting zone between the Baltic and the North Seas known as the halocline [3,4]. Along the halocline surface water salinity on the North Sea side of the halocline at Kattegat is about 34–35 g/L [4] and the salinity at surface on the Baltic side is about 8 g/L [3]. Energy production by PRO has also been proposed via harnessing the salinity difference between the Dead-Sea and either the Red Sea or the Mediterranean Sea [5].

Energy production via PRO requires adequate water permeation across the PRO membrane from low (feed) to high (draw) salinity streams and higher hydraulic pressure in the draw than that in the feed channels. The generated power (expressed as power density in units of W/m^2), under ideal conditions (neglecting all losses and assuming ideal pumps and energy recovery devices), is approximated [6] as $W = J_w \Delta P$ (where J_w and ΔP are the average water flux and transmembrane pressure). For the above ideal conditions, the maximum peak power generation is $W_m = A \cdot \Delta\pi^2/4$ (where A is the membrane water permeability and $\Delta\pi$ is the transmembrane osmotic pressure difference). Peak power generation [7–9], for a given membrane and channel geometries and stream salinities, is dictated by the PRO operating conditions (i.e., imposed hydraulic pressure, cross flow velocities). The latter govern the concentration field development and salt back diffusion and associated reduction in the water permeation driving force [10,11]. Bench-scale experimental PRO studies, which have generally been carried out with short PRO channels (typically ~8–15 cm, [9,12–14]), have shown that PRO power generation increases with membrane permeability and draw solute concentration but decreases with feed concentration and the membrane length. It is important to recognize that PRO power generation may be more significantly impacted by concentration polarization (CP), salt back diffusion and

* Corresponding authors.
E-mail addresses: yoram@ucla.edu (Y. Cohen), cesemiat@technion.ac.il (R. Semiat).

http://dx.doi.org/10.1016/j.desal.2016.09.015
0011-9164/

frictional pressure losses with increased channel length. For example, modeling studies, utilizing the 1-D film model, along with various approximations [13,15], concluded that due to CP one should expect up to about 10% flux decline [15] in long membrane channels (~1 m) and 40% lower power generation than attained in short laboratory channels [13].

The majority of PRO studies have relied on process analysis based on the one-dimensional film model (assuming fully developed axial flow and concentration fields) [2,16–18]. In these studies the PRO membrane has been characterized by the water permeability and salt transport coefficient, denoted by A and B, respectively, and the PRO membrane porous support structural parametert S (i.e., $S = t_s\tau/\varepsilon$, in which t_s, τ and ε are the support layer thickness, tortuosity and porosity, respectively). Various studies have argued [13,19–21] that the PRO membrane support layer represents the major resistance to water permeation due to internal CP (i.e., ICP). For example, it was reported [2] that by tuning the support layer thickness to be in the range of 70–100 μm and with S ≤ 0.5 mm it may be possible to achieve power density higher than 5 W/m^2 which is often cited as an acceptable level for PRO power generation [9]. It is noted that various studies on osmotically-driven FO [10,20] have also concluded that the support layer offers greater resistance to water permeation compared to both the active membrane layer and external CP (in the feed and draw channels). In contrast, recent forward osmosis (FO) studies [20,22,23] have presented detailed analysis, relying on CFD models in conjunction with reported literature data, demonstrating that the membrane active layer and external CP layers represent a far greater resistance to water permeation relative to the support layer.

Previous PRO studies have also documented that power generation, for a given specific feed and draw streams, PRO membrane type, and height and lengths of the draw and feed channels, is highly dependent on the crossflow velocities of the PRO draw and feed streams [7,24]. The above should be expected since the crossflow velocities in the feed and draw channels will impact both external concentration polarization (ECP) and internal concentration polarization (ICP), as well as frictional pressure losses. Accordingly, in the present work a systematic approach is presented, making use of a detailed 2-D FEM model of the coupled hydrodynamics and mass transfer equations, to explore the impact of PRO operating conditions on the attained maximum level of power generation. The present analysis considers feed and draw channel frictional pressure losses, feed pumping energy and efficiency of PRO hydraulic to energy conversion, as well as the influence of membrane channel height and length, in addition to potential improvements that may be afforded by increasing membrane permeability. Specific examples of the attainable PRO power production are then presented for the draw/feed combinations of seawater/brackish-water, RO-concentrate/brackish-water and Dead-Seawater/RO-concentrate.

2. Modeling of pressure-retarded osmosis

2.1. Work flow for maximizing osmotic power generation

The maximum osmotic power that can be generated via PRO, for a given feed and draw streams, specific PRO membrane type, and RO channel height and length, was first evaluated consisted of the major steps as per the workflow described in Fig. 1. In the first step membrane water permeability and salt transport parameters should be extracted from suitable experimental PRO membrane performance data. In the present illustration of the approach, membrane transport parameters were extracted from available literature bench-scale data using a 2-dimensional (2-D) CFD model (Section 2.2) following the method described in [23,25]. Subsequently, for specific feed and draw streams and prescribed PRO feed and draw channels (i.e., of a prescribed height and length), an iterative process is followed to find the inlet draw stream velocity that will maximize the peak power generation; here, one must recognize that utilization of the feed stream should be sufficiently high in order to maximize the energy that can be extracted for a given draw stream volumetric inflow rates. In other words, for each selected inlet draw stream cross flow velocity there should be a corresponding inlet feed stream velocity that will result in high level of feed stream utilization. Accordingly, for a selected draw steam velocity the CFD model is solved iteratively varying the feed inlet cross flow velocity, $V_{f,in}$, until a solution is reached whereby the feed channel outlet feed crossflow velocity, $V_{f,out}$, vanishes to within a tolerance level, i.e., $0 < V_{f,out}/V_{f,in} < \varepsilon$, which signifies near complete utilization of the feed stream. The above process is repeated for different values of inlet draw stream velocity in order to determine the stream velocities that maximize the peak power generation. It is emphasized that the CFD model solution for the above considers both ECP and ICP as well as frictional pressure losses. Following the above analysis, the impacts of channel length and height on the attained maximum energy production is evaluated first considering PRO operation with ideal (i.e., 100% efficient) feed pumps and hydraulic energy recovery devices (ERD). Subsequently, we estimate the reduction in net PRO power generation due to the use of non-ideal pumps and ERDs (i.e., efficiencies < 100%) in addition to the effect of frictional pressure losses.

2.2. PRO fluid flow and mass transport

In the PRO process high salinity (draw) and low salinity (feed) salt solutions, which flow through a draw and feed channels, respectively, are separated by a semi-permeable membrane (Fig. 2). The feed solution is fed on one side of the membrane and water then permeates through the membrane to the draw channel side. The draw solution is maintained under pressure which is set below the draw osmotic pressure. The energy gained is the product of the added water flow rate on the draw side (via permeation from the lower salinity feed channel) and the draw stream exit pressure. The available hydraulic energy is then converted (or recovered) using a suitable energy recovery device (ERD; e.g., turbine or pressure recovery device). In determining the net energy gain, however, one must account for any energy expenditures due to pumping of the draw and feed streams and any frictional energy losses in the membrane channels.

Water permeation across the PRO membrane (from feed to draw side) is governed by the osmotic pressure and hydraulic pressure differences. Countercurrent flow is typically utilized where the hydraulic pressure is higher in the draw channel relative to the feed channel. In the present analysis, the development of the flow and salt concentration fields along the channels, permeate flux and power generation were determined from numerical solution of the 2-dimensional (2-D) CFD model consisting of the coupled hydrodynamic and mass transfer governing equations.

The hydrodynamics in the feed and draw channels, for the case of 2-D steady-state flow, is described by the Navier-Stokes equations of motion and the continuity equation,

$$\boldsymbol{u}_i \cdot \nabla \boldsymbol{u}_i = -\frac{1}{\rho_i}\nabla p_i + \nabla \cdot \left[\nu_i(\nabla \boldsymbol{u}_i + (\nabla \boldsymbol{u}_i)^T\right], \qquad \nabla \cdot \boldsymbol{u}_i = 0 \tag{1}$$

in which the subscript i denotes either the feed ($i = f$) or draw ($i = d$) channels, and the solutions density and kinematic viscosity are denoted by ρ_i, ν_i, respectively. The pressure term $p_i = P_i - P_{io}$ represents the difference between the actual applied pressure P_i and the pressure P_{io} at the outlet of the channel. The 2-D differential operator, $\nabla \equiv (\partial/\partial x, \partial/\partial y)$ is along x and y being the coordinates normal to the membrane surface and in the cross flow direction, respectively, and $\mathbf{u}_i$ is the velocity vector in the x, y domain. The axial velocity in the support layer at $y = 0, L$ is set to zero and the velocity profile at the channel entrance (i.e., $y = 0$) was taken as parabolic. Within the porous support layer the flow field is described by the Brinkman's equation [26],

$$\frac{\eta}{\kappa}\boldsymbol{u} = -\nabla p + \frac{1}{\varepsilon_p}\nabla \cdot \left[\eta(\nabla \boldsymbol{u} + (\nabla \boldsymbol{u})^T\right], \qquad \nabla \cdot \boldsymbol{u} = 0 \tag{2}$$

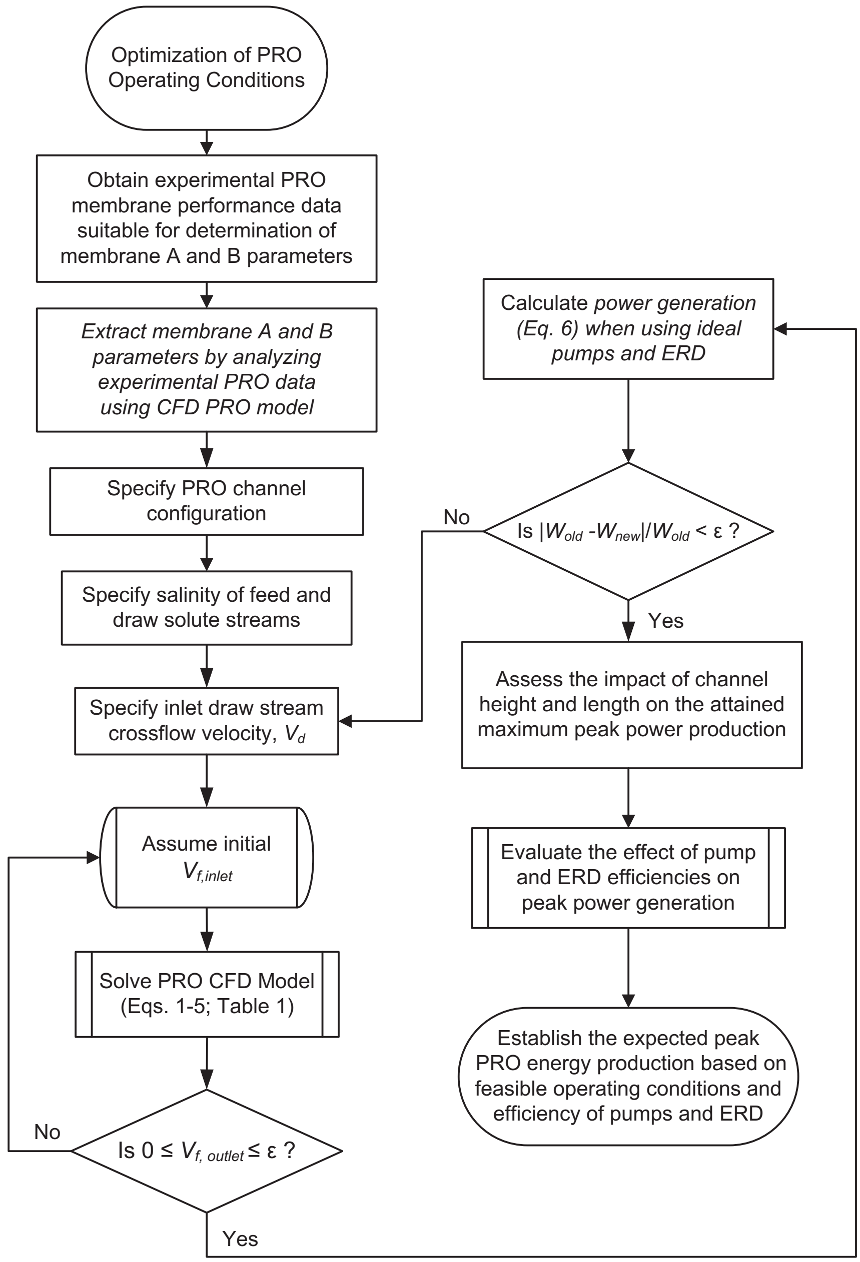

Fig. 1. Work flow for evaluating the impact of various factors on PRO energy production.

where κ and ε_p are hydraulic permeability of the support layer and its porosity, respectively.

Salt transport in the feed and draw channels and the support layer is described by the convection and diffusion equations [26],

$$\nabla \cdot \left(D_{k,i} \nabla c_{k,i}\right) = \boldsymbol{u}_{k,j} \cdot \nabla c_{k,i} \tag{3}$$

in which index i refers to either the feed channel ($i = f$), porous support ($i = p$) or draw channel ($i = d$), and where subscript k represents the solute. The mass diffusivity of solute k is denoted by $D_{k,i}$, and where in the porous support $D_{k,p} = D_k \cdot \varepsilon_p / \tau$, in which τ is the porous layer and D_k is the solute mass diffusivity in the solution.

The draw and feed solutions enter the PRO channels at salt concentrations of $C_{d,i}$ and $C_{f,i}$, respectively, and the velocity profiles at the entrance to the two channels are taken to be laminar. Water permeates from the feed to the draw channel and the local flux is given as [2],

$$J_w = A \cdot \left[(\pi_d - \pi_p) - (P_d - P_f)\right] \tag{4}$$

in which A is the membrane intrinsic water permeability, π_d and π_p are the solution osmotic pressures at the membrane active layer surfaces at the draw and feed-sides, respectively, The hydraulic pressures P_f and P_d are in the feed and draw channels, respectively, where the corresponding hydraulic pressures in the draw and the feed channels are given as $P_d = p_d + P_{do}$ and $P_f = p_f + P_{fo}$. The outlet pressures in the draw and feed channels are denoted by P_{do} and P_{fo}, respectively, and the pressures difference variables p_d and p_f are those used in Eqs. (1) and (2). Solute flux (across the membrane) from the draw to the feed channel is described by,

$$J_s = B \cdot \left(C_d - C_p\right) \tag{5}$$

in which B is the intrinsic salt transport coefficient, c_d and c_p are draw and support concentrations on both sides of the membrane skin surfaces. Additional boundary conditions listed in Table 1 and referenced in Fig. 3, which are necessary for the solution of the model Eqs. (1)–(3), include symmetry, no-slip ($\mathbf{u}_i = 0$) and solute no-flux

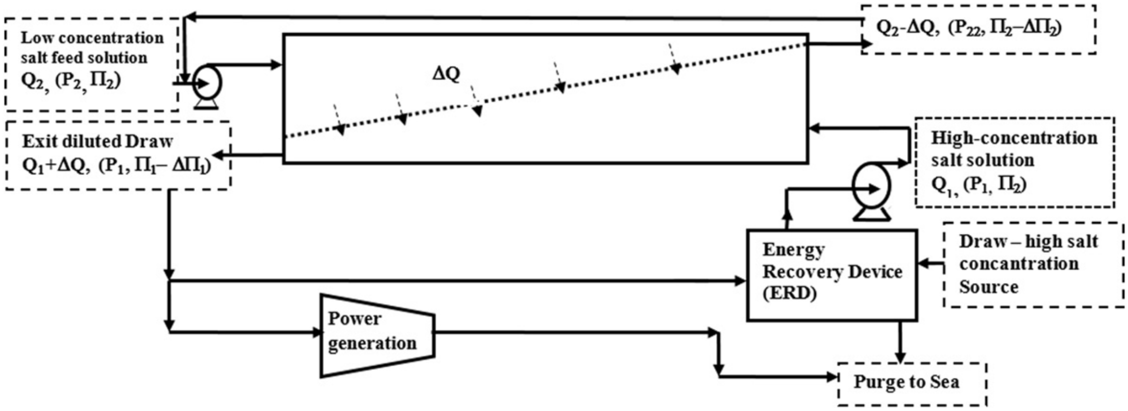

Fig. 2. Schematic view of a PRO process. High salt concentrated solution (e.g., seawater) is fed to the draw side into the energy recovery device that increases its pressure, followed by a pump that elevates the needed high draw pressure of the draw solution. On the other side, low concentration salt stream (e.g., brackish water) is delivered to the feed side of the membrane via a low pressure pump. This stream transfers water through the membrane and exits at a lower flowrate, lower pressure and higher osmotic pressure. The draw solution flowrate is increased by the accumulated water flux, its osmotic pressure decreases and pressure is also reduced. This stream is divided into two streams, one passing through a turbine (or another ERD type) to recover the gained energy and the main stream which exchanges its pressure with the entering concentrated draw solution.

conditions (insulation or impermeable wall, $J_s = 0$), and viscous stress and pressure conditions at the channels [26].

Eqs. (1)–(7), PRO channel dimensions and associated boundary conditions (Table 1) constitute the PRO 2-D CFD model (Fig. 3). Model input parameters include the following concentration-dependent parameters: dynamic viscosity (η), density (ρ), osmotic pressure (π), and solute mass diffusivity (D). Additional parameters included solution permeability (κ) through the porous support, porous support layer porosity (ε_p) and tortuosity (τ), and membrane water permeability (A) and salt transport parameter (B). In the present study, the parameters A and B were extracted from experimental membrane performance data (Section 3.1 and Appendix A, Section A.1), using the CFD transport model, as described elsewhere [23,25].

The net power generation, W_n (expressed as power generation per membrane area, i.e., power density, W/m^2), derived from the PRO process, accounting for internal pressure losses in the draw and feed channels and efficiencies of feed pumps and energy recovery device (ERD) [9] is calculated from:

$$W_n = J_w P_{d,o}\eta_{E,d} - \left[\frac{Q_{d,i}}{S_m}\left(\frac{P_{d,i}}{\eta_H} - P_{d,o}\eta_{E,d}\right) + \frac{Q_{f,i}}{S_m}\frac{P_{f,i}}{\eta_L}\right] \tag{6}$$

where Q, and P are the volumetric flowrate and pressure, average flux J_w along the membrane channel, indices d, f designate the draw and feed streams respectively and i, o denote the channels inlet and outlet, respectively, and where feed outlet is taken to be at atmospheric pressure. The efficiencies of the draw (η_H) and feed (η_L) high and low pressure pumps, respectively, are expected to be in the range of 0.6–0.8 [27,28], and efficiency of energy recovery devices (e.g., turbines), η_E, at the high end is in the range of ~0.90–0.96 [29]. Here it is noted that the condition of $\eta_E = 1$ and $\eta_H = \eta_L = 1$ would represent an ideal scenario which is unlikely to be realized in practice. Moreover, given the added pressure added losses due to channel spacers, the pressures $P_{j,o}$ at the feed and draw channel outlets is reduced as expressed below,

$$P_{j,o} = P_{j,i} - \Delta P_{j,loss} \tag{7}$$

in which $j = f$ for feed and $j = d$ for draw and where $\Delta P_{j,loss}$ represents the pressure loss in the channels (draw or feed) calculated (Appendix A, Section A.2) following the method of [30] which accounts for channel spacers. This approach was taken since CFD analysis of PRO with channel spacers is computationally prohibitive given the need for iterative simulations to arrive at the optimal operating conditions. Nonetheless, the present approach provides a reasonable estimate of the expected pressure losses.

Once the permeate flux is determined for a given PRO channels geometry and operating conditions, the net power generation, W_n, can be calculated via Eq. (6) accounting for pressure losses as per [30]. The cross flow velocities of the feed and draw streams, V_f and V_d, respectively, affect the net achievable power density, W_n, given that pumping of both the feed and draw solutions is likely to require energy input. Therefore, the minimal inlet applied feed pressure required for maintaining

Table 1
Boundary conditions[(a)] for the PRO 2-D system with SFD/counter-current configuration shown in Fig. 3.

Boundary[(a)] #	Navier-Stokes equations			Convection-diffusion equation		
	Feed	Porous	Draw	Feed	Porous	Draw
1	Symmetry[(b)]	–	–	Symmetry[(e)]	–	–
2	Outlet[(c)]	–	–	Outlet[(f)]	–	–
3	Inlet v_f	–	–	*Inlet* c_{f0}	–	–
4	Outlet J_w	Inlet J_w	–	$c_f = c_p$	$c_p = c_f$	–
5	–	Wall[(d)]	–	–	No flux	–
6	–	Wall[(d)]	–	–	No flux	–
7	–	Outlet $J_w J_w$	Inlet J_w	–	Inlet J_s	Outlet J_s
8	–	–	Inlet v_d	–	–	*Inlet* C_{d0}
9	–	–	Outlet[(c)]	–	–	Outlet[(f)]
10	–	–	Symmetry[(b)]	–	–	Symmetry[(e)]

[a] Boundary numbers are defined in Fig. 3. Details of the mathematical expressions for the boundary conditions are provided in [26].
[b] Zero velocity normal to the plane of symmetry.
[c] Zero viscous stresses and zero applied pressures p_f and p_d.
[d] No slip condition or zero velocity.
[e] Zero convective flux normal to the symmetry plane.
[f] Vanishing (within a prescribed tolerance, See Section 2.1) axial convective fluxes at the feed channel outlet.

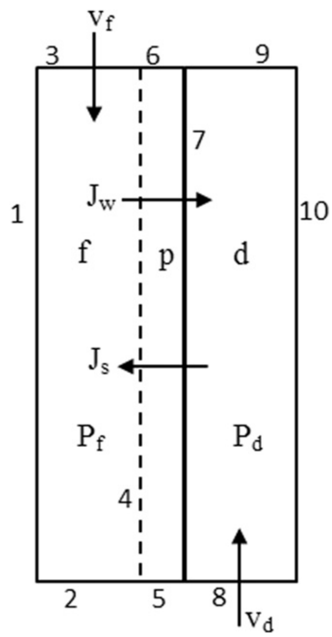

Fig. 3. Schematic diagram of a PRO unit operation in the skin-facing-draw (SFD)/counter-current mode. The half channels to the left and right are of the feed and draw channels, respectively, denoted by the corresponding subscripts *f* and *d*, and where the middle zone (denoted by subscript *p*) represents the porous support. (Note: the numbers correspond to the specific boundary conditions listed in Table 1).

the feed flow was set as $P_{f,in} \approx P_{f,loss}$ [9]. Furthermore, in order to assess the beneficial impact of developing membranes of higher permeability than the current generation of PRO membranes, simulations were also conducted over a wider range of membrane permeability (A) and salt transport coefficient (B). Also, since pump and ERD efficiencies reduce the obtained net power, in the present approach simulations are first conducted searching for the PRO operating conditions that maximize the net power production for ideal conditions (i.e., 100% efficiencies of feed pumps and ERD). Subsequently, the impact of feed pumps and ERD efficiencies on the net power generation is determined to assess the practically achievable osmotic power production.

2.3. Simulations

In order to evaluate the influence of various PRO operational factors on the feasible level of osmotic energy extraction it is necessary to first establish the membrane transport parameters (A and B). In the present study, as per the approach summarized in Fig. 1 and outlined in Section 2, simulations were conducted based on PRO membrane of water permeability (A) and salt transport coefficient (B) as determined from experimental bench-scale PRO data (Appendix A). Accordingly, the PRO model equations (Section 2.2) were solved via the finite-element approach [26] seeking the membrane parameters that lead to best matching of the experimental and calculated salt fluxes with deviations of <3.3% and 9.8% for J_w and J_s, respectively. The extracted A and B values (Appendix A, Section A.1), were then utilized in simulations to arrive at the inlet feed and draw streams crossflow velocities that would maximize PRO power generation for a 1 m long channel (Table 2) which is about the length typically expected in commercial deployment [6]. Using the PRO model (Section 2.2), PRO analysis was subsequently carried out for feed and draw solutions of salt concentrations that reflect the salinity levels for brackish water and brine from seawater desalination (i.e., RO concentrate), as well as Dead Sea water as draw for PRO; the latter has been proposed for commercial deployment of PRO power generation [31].

Simulations were carried out with mesh density that increased from the bulk toward the membrane surfaces. For short PRO channels the element density was set at ~560 elements/mm^2 in proximity of the membrane surface and close to the channels ends and decreased to ~110 elements/mm^2 toward the channel center and near the walls. The mesh density was doubled for the long channel simulations. Grid size independence of the numerical solution was evaluated for all simulations as per the convergence criterion described in [23], whereby global convergence was ascertained when the calculated water flux did not significantly change (<0.001%) upon doubling the mesh density.

Table 2
PRO simulation parameters.

Parameters	Values	Description
L, W	1 m	Length and width for a commercial scale membrane
ε, K	0.77, $1.5 \cdot 10^{-11}$ m^2	Support porosity [32], permeability [33]
d_f, d_d	$7.11 \cdot 10^{-4}$ m[(a)]	Feed and draw channels heights [34]
t_s	$7.62 \cdot 10^{-5}$ m	Membrane support layer thickness [7]

[a] Nominal value. The impact of channel height was assessed for the range of $5.08 \cdot 10^{-4}$ m - $1.168 \cdot 10^{-3}$ m [34].

3. Results and discussion

3.1. Determining the draw and feed stream cross flow velocities that maximize the net power production for the case of ideal pumps and energy recovery device (ECD)

The approach to assessing the operating conditions that will maximize PRO net power generation was demonstrated for a membrane having the specific membrane transport parameters extracted from the experimental data in [7]. This dataset was selected given the relatively high power density ($W = 12.8$ W/m^2) reported, along with corresponding water and salt flux data. Extraction of the membrane A and B parameters from the dataset revealed those parameters to be pressure dependent (Appendix A, Section A.1). Subsequently, assessment of the maximum attainable power production for a long (1 m) channel (Table 2) proceeded with the net power density (W_n) calculated considering pressure losses (Eqs. (6) and (7), and Appendix A, Section A.2) while also assessing the impact of pumps and ERD efficiencies.

The generated power production has a maximum with respect to the applied pressure difference (Fig. 4) as expected for the PRO process

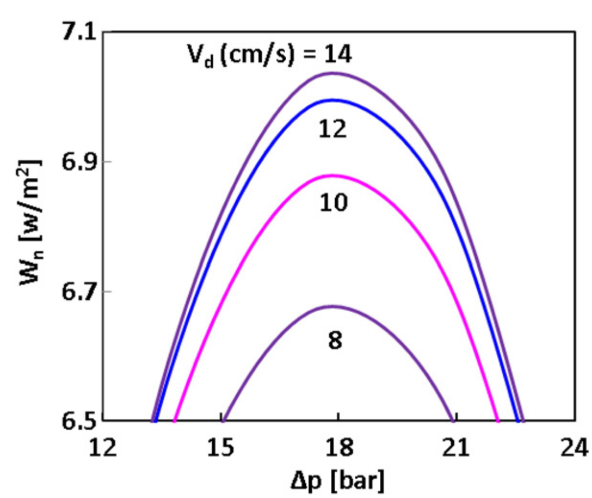

Fig. 4. Net power generation (W_n, W/m^2) dependence on hydraulic pressure difference (Δp, bar) for different inlet draw stream cross flow velocities with (solid lines) and without (dashed lines) consideration of pressure losses, and ideal (i.e., 100% efficiency) pumps and ERD. Simulation conditions: membrane A and B transport coefficients were extracted from the data of [7] (Fig. 4, PEI 2# membrane), PRO channel of 1 m in length and height of 0.71 mm. Feed and draw solutions inlet salt (NaCl) concentrations were set at 10 mM and 1 M, respectively. The outlet feed crossflow velocity, V_f, was determined to be about 0.55 cm/s for feed inlet velocity range of ~6 cm/s for the above range of inlet draw stream velocities (i.e., 10–14 cm/s).

[7,35]. The above behavior is depicted in Fig. 4 for the case of feed and draw solution being at NaCl concentrations of 10 mM and 1 M, respectively, representing low salinity brackish water or treated tertiary wastewater and seawater RO brine. Power production (expressed as power density) for a long membrane (1 m) under the ideal case (i.e.,$W = J_w \Delta P$, where $J_w = A(\Delta\pi - \Delta P)$ and constant A (set as the average value from Fig. A1) was higher by a factor of 4.8 and 4.2 than predicted by the CFD model with and without pressure losses, respectively, assuming pumps and ERD of 100% efficiency. The above behavior is not surprising considering that the CFD model accounts for the decline in osmotic pressure driving force (due to concentration polarization and salt back diffusion) and channel frictional pressure losses. As the draw stream crossflow velocity increases, the impact of CP decreases which tends to elevate the level of energy production; however, frictional pressure losses increase with increased crossflow velocity (Appendix A, Section A.2). As a consequence, a maximum achievable peak net power generation is expected with respect to the draw stream cross flow velocity (Fig. 5). For example, as shown in Figs. 4 and 5 the peak power density increases by 1.7% (from 6.89 to 7.01 W/m^2) as the draw stream velocity, V_d, increases from 10 to 12 cm/s (20%) with an additional 0.6% net peak power density increase as V_d further rises by additional 16.6% (to 14 cm/s).

3.2. Impact of PRO channel length and height on the attainable net peak power production

Frictional losses, concentration polarization and salt back diffusion, which are all impacted by PRO channel length and height, reduce the attainable PRO energy generation. As an illustration, the impacts of channel length and height are shown in Fig. 6, for the case of ideal pumps and hydraulic energy recovery device (i.e., 100% efficiency) and draw and feed solutions as in Fig. 5 at inlet draw and feed velocities of 14 cm/s and 6 cm/s, respectively. As seen in Fig. 6, the net PRO power density is marginally impacted by the channel dimensions. For a given crossflow velocity, thinner channels will develop thinner ECP (given the higher fluid shear rate at the channel fluid/membrane interface) and thus higher water flux and correspondingly higher W_n. However, pressure losses can increase significantly for thin channels once one accounts for the impact of spacers. For example, relative to a PRO channel of 1 m in length and 0.71 mm height, decreasing the channel height to ~0.5 mm (i.e., by ~29%), for a given crossflow velocity, would result in minor power density gain of ~4% (i.e., from 7.3 W/m^2 to ~7.6 W/m^2).

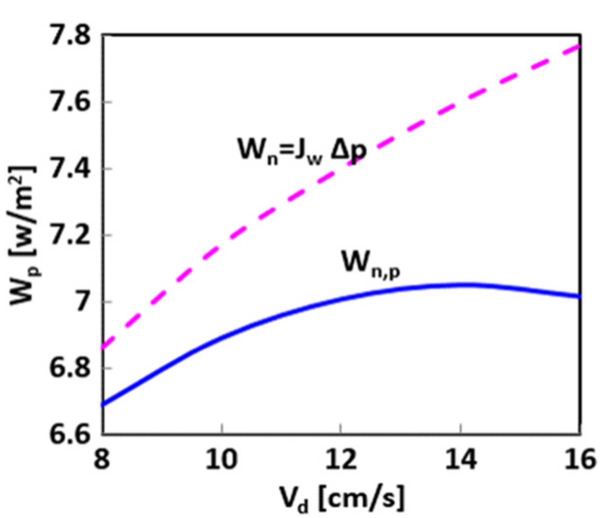

Fig. 5. Variation of peak power, $W_{n,p}$ (W/m^2), with (solid line) and without (ideal case, $W_n = J_w \cdot \Delta p$; dashed line) frictional pressure losses (for 100% efficient pumps and ERD) with the inlet draw stream cross flow velocity (V_d) for the simulation scenario of Fig. 4. The maximum net peak power is $(W_{n,p})_{max} = 7.05$ W/m^2 at $\Delta p = 18.1$ (bar) for inlet draw and feed stream velocities of 14 cm/s and 6 cm/s, respectively.

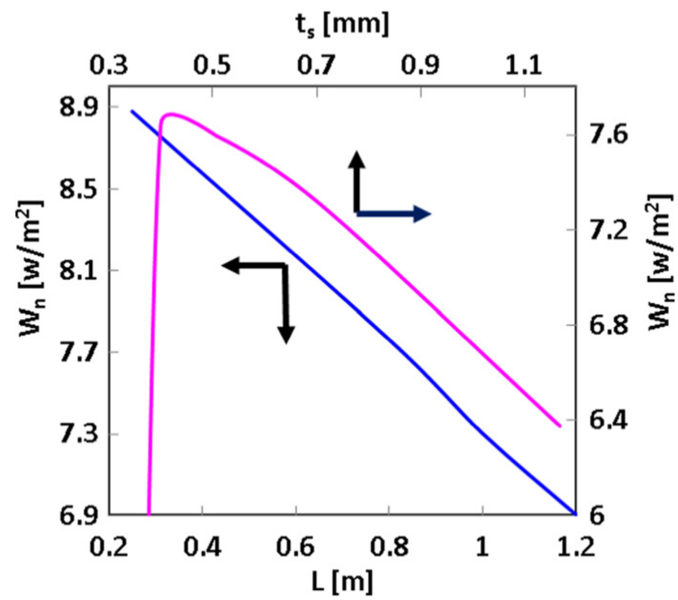

Fig. 6. Variation of PRO peak energy generation with channel length and height (taken to be identical for the draw and feed channels), for feed and draw solutions as in Fig. 4, at inlet draw and feed stream crossflow velocities of 14 cm/s and 6 cm/s, respectively, that produce the maximum peak energy production considering frictional pressure losses (for spacer-filled channels) assuming ideal (i.e., 100% efficient) pumps and ERD. Simulations with respect to channel length were for a channel height of 0.71 cm. Note: peak power generation was achieved at $\Delta p = 18.1$ bars.

As the channel height of ~0.4 mm is reached, a maximum peak power density is attained which decreases rapidly with further decrease in channel height. Simulations for lower channel height down to 0.35 mm would result in a vanishingly low level of power generation, when compared at the same crossflow velocity, given the low flow rate which cannot sustain the required flux. Frictional pressure losses increase with channel length (i.e., lower pressure loss for shorter channels; Appendix Section A.2). For example, decreasing the membrane length from 1 m to 0.5 m or 0.25 m would increase the energy density (relative to power density of ~7.3 W/m^2 for 1 m long channel) by ~13% and 33%, respectively. Here it is noted that the use of shorter membrane elements could increase capital cost (due to increased number of membranes, fittings, valves, etc.); therefore, the selection of membrane element length is clearly a decision that would involve economics and engineering considerations.

3.3. Effects of membrane permeability (A) and salt transport coefficient (B)

An assessment of the impact of increasing membrane permeability (A) and decreasing salt transport (B) on the level of PRO energy generation is illustrated in Fig. 7 for the case of the draw/feed streams as in Fig. A1 (Table A3 in Appendix A), representing the case mimicking Seawater RO concentrate/low salinity brackish water as draw/feed streams), for the channel dimensions given in Table 2, considering frictional losses but with ideal pumps and ERD and crossflow velocities as in Figs. 4–6. For the purpose of the present illustrative analysis, the achievable peak PRO energy density was estimated considering constant A and B values relative to the corresponding nominal values of $3.8 \cdot 10^{-12}$ m/sPa and $5.1 \cdot 10^{-7}$ m/s (i.e., the intrinsic A and B values derived from [7] (Fig. A1, Appendix A). Such analysis is somewhat speculative since information on the variation of salt transport coefficient relative to water permeability is unavailable for membranes of characteristics removed from the nominal values of the presented analysis. Notwithstanding the above, as expected (Fig. 7a) higher A would lead to higher water flux and thus higher attained power peak density. As demonstrated in Fig. 7a, there is a sharp increase in energy production, by up to a factor of ~2.75, as the ratio A/A_{int} increased from 1 to 10. For

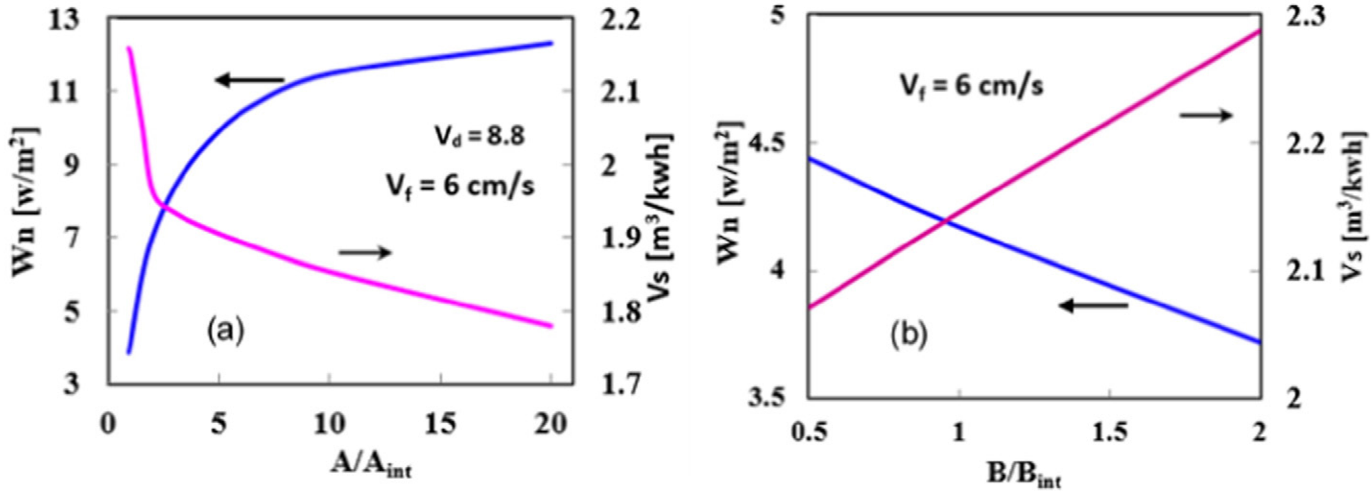

Fig. 7. (a): The impact of increasing membrane permeability (A) on peak power generation, and (b) Effect of salt transport coefficient (B) on peak power generation expressed as both energy density (based on membrane area), W_n, and feed water volume utilized per unit energy produced (m^3/kWh) denoted as V_s. Simulation are shown for the case of SWB/BW draw/feed streams for constant A and B values with $B = B_{int}$ in 7(a) and $A = A_{int}$ for 7(b) considering ideal pumps and ERD and crossflow velocities that maximize peak power generation for the channel dimensions as in the simulation scenario of Fig. 4. (Note: A_{int} and B_{int} are $3.8 \cdot 10^{12}$ m/s and $5.1 \cdot 10^{-7}$ m/s, respectively, based on analysis of the data in [7].

given inlet cross flow velocities, higher flux (i.e., due to higher A) would increase the adverse impact of CP. Therefore, one should expect that power production will reach a maximum with respect to membrane permeability. Although the present analysis was only conducted up to $A/A_{int} = 20$, it is clear that beyond A/A_{int} ~10 there is only marginal (<7.3%) increase in the peak energy production.

As the salt transport coefficient (B) increases back-diffusion of salt from the draw to the feed channel becomes more pronounced leading to reduced osmotic pressure driving force for water permeation and thus lower power production (Fig. 7b; Appendix B). Clearly, PRO membranes of low B are desired in order to increase energy production. For example, as B/B_{int} decreases by a factor of 2 (from a value of 1 to 0.5) energy production will increase by only 6.4%. Of course, increased salt passage (reflected by increased B/B_{int}) will lead to reduction in energy production (e.g., by 10.8% as B/B_{int} decreases by a factor of 2 relative to the base value) given the associated reduction in the osmotic pressure driving force for water permeation. It is also noted that, over the wide range of A and B values, a feed volume of about 2 m^3 is required for the extraction of 1 kWh of osmotic energy from seawater RO brine (SWB). It is interesting to note that the osmotic energy available in seawater (of ~35,000 mg/L total dissolved solids) for mixing with river water is about 0.79 kWh/m^3 [36]; thus, a reversible process of osmotic energy extraction would require about 1.25 m^3 of pure feed water. Overall, the above example and results of Section 3.2 suggest that the level of energy production from seawater RO brine/fresh water, even for membranes that would be significantly higher than the current generation of PRO membranes and with ideal pumps and ERD, is likely to be below 0.5 kWh/m^3.

3.4. Estimation of power density for PRO with seawater and Dead-sea water

The feasible range of net PRO power production was assessed for possible use of feed/draw stream combinations consisting of seawater (0.6 M)/low salinity brackish water (0.01 M) (SW/BW), seawater RO brine (1 M)/brackish water (SWB/BW) or Dead Sea water (5.8 M)/seawater RO brine (DSW/SWB). The above were selected in order to cover the range of potentially available natural feed/draw solute salt streams. For the purpose of demonstrating the impact of pumps and ERD efficiencies, PRO power generation for the above combinations of draw/feed streams was carried out with the draw stream and feed stream velocities of 14 cm/s and 6 cm/s (Section 3.1) that were assess to maximize the peak energy production for the SWB/BW case with a channel length and height of 1 and 0.71 cm, respectively (Table 2). The intrinsic membrane permeability (A) and salt transport coefficient (B) were respectively taken to be $3.85 \cdot 10^{-12}$ m/(s·Pa) and $5.4 \cdot 10^{-7}$ m/s as determined from Fig. A1 (Appendix A), with support layer thickness, porosity and permeability being 76.2 µm, 0.77 and 1.08×10^{-11} m/(s·Pa), respectively [7].

The peak power density that can be generated via PRO from the above SW/BW, SWB/BW and DSW/SWB draw/feed water streams were determined, from CFD model simulations and using Eq. (6), to be 3.53 W/m^2, 7.29 W/m^2, and 35.3 W/m^2, respectively, for the case of ideal pumps (i.e. $\eta_p = 1$) and ERD (i.e., $\eta_E = 1$). The peak power density decreased linearly with decreasing pump and ERD efficiencies as illustrated in Figs. 8–9. It is noted, that for high end ERD efficiency ($\eta_E = 0.96$; [29]) and ideal pumping efficiency ($\eta_p = 1$) the peak power density expected from DSW/SWB PRO is 19 W/m^2. The results of Fig. 9 illustrate that ERD efficiency would have to be above 0.91, 0.92 and 0.95, for the DSW/SWB, SWB/SW and SW/BW draw/feed streams, in order for the PRO process to provide net positive peak energy production even with the use of ideal pumps ($\eta_p = 1$). Similar analysis reveals that, for the case of an ideal ERD ($\eta_E = 1$), the minimum pump efficiency required to achieve positive net peak power production for the DSW/SWB, SWB/BW and SW/BW draw/feed streams is 0.91, 0.92 and 0.96, respectively. As shown in Fig. 9, for the case of high efficiency ERD ($\eta_E = 0.96$, [29]), even the most optimistic scenario of high PRO energy productivity for DSW/SWB with commercially available high efficiency pumps (i.e., $\eta_p = 0.98$, [27,28]), the maximum peak power density is not likely to exceed ~12 W/m^2 and 2 W/m^2 for the DSW/SWB and SWB/BW cases, respectively, while essentially no power generation is expected for the SW/BW case.

It is instructive to quantify the sensitivity of PRO peak power generation (at the optimal conditions that maximize power production) with respect to pump and ERD efficiencies for the three different feed/draw streams evaluated. Accordingly, one can express the change in the maximum peak power generation as $\Delta W_i = \alpha_i \Delta(\eta_i)$ where α is a sensitivity coefficient and the subscript i denotes either the system pumps or ERD. These sensitivity coefficients are essentially the slopes of the net energy production versus efficiency in Figs. 8 and 9. Accordingly, 1% change in pumping or ERD efficiencies would result in the peak power generation as listed in Table 3 demonstrating that improvements in power generation by pump or ERD efficiencies will be more significant for the DSW/SW draw/feed combination. The power generation gain by increasing pump efficiency will be marginal for the SWB/BW and SW/BW given that relatively high pump and ERD efficiency are required (Fig. 9) for net power generation. Likewise, increasing ERD efficiency beyond 92%

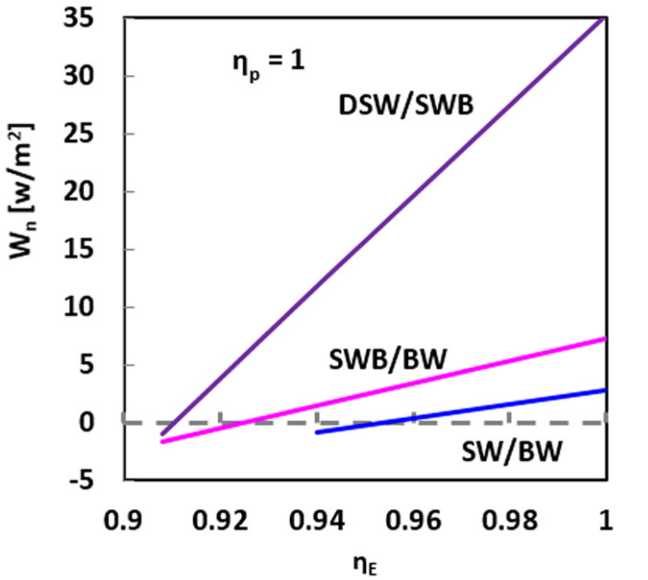

Fig. 8. Variation of net energy production (W_n) with energy recovery efficiency (η_E) for the case of ideal pumps ($\eta_p = 1$) for the draw and feed velocities of 14 cm/s and 6 cm/s, respectively that maximize the net peak power production. Simulations were for feed and draw channel geometries as listed in Table 2. (DSW – Dead Sea water, SW – Seawater, SWB – Seawater RO brine, BW – brackish water).

and 95% for SWB/BW and SW/BW are required with essentially ideal pumps for reasonable net energy production. The above analysis suggests that only the case of DSW/SWB could possibly provide reasonable net energy production (e.g., ≥5 W/m^2 [37]) but this provided that pumps of high efficiency (e.g., well above 90%) would be available and with ERD efficiency of ~98% and preferably higher.

3.5. Implications of parameter estimation with respect PRO performance assessment

The present PRO process analysis was based on fundamental treatment that considers the coupling of fluid flow and mass transfer whereby membrane transport parameters and other relevant geometrical channel parameters are extracted from experimental data reported in the literature. It is noted, however, that fundamental membrane transport parameters and accompanying PRO performance data are generally reported based on experiments performed in small PRO cells of short channel length and small membrane coupons. In such studies, the crossflow velocities of the draw and feed streams in the channels are often higher than the optimal range that would maximize the produced energy while not revealing the excessive frictional pressure losses that would be otherwise experienced in longer channels. Also, the channel heights in bench scale systems are usually high to the extent that channel Reynolds numbers are higher (often ≥1000) [10,20] than one would expected for a PRO process operating under optimal conditions (e.g., those required for high utilization of the feed volume). It is noted that bench-scale laboratory PRO data were readily available in the literature for seawater/freshwater PRO evaluation of specific membrane transport properties. In contrast, literature PRO data were insufficient or unavailable for higher concentration feed and draw streams. Therefore, in the present analysis, the values of *A* and *B* utilized for the high concentration streams (e.g., seawater RO brine and Dead Sea water) were taken to be those extracted for the lower concentrations. In this regard, it is expected that membrane water permeability would be expected to be lower and salt passage higher for the above higher concentration feed and draw streams. As a consequence, the present estimation of PRO performance with respect to energy extraction from seawater, seawater RO brine and Dead Sea water is expected to be overly optimistic with regard to the level of attained power production.

It is known that increased crossflow velocity in the feed and draw channels will reduce concentration polarization which in turn reduces water permeation across the membrane. However, increased velocity

Table 3
Sensitivity of the extracted osmotic power with respect to pump and ERD efficiencies.

Pump or ERD Efficiency	Sensitivity due to:	DSW/SWB	SWB/BW	SW/BW
$\eta_p = 1$	1% change in η_E	3.92	0.974	0.607
$\eta_E = 1$	1% change in η_p	3.96	0.980	0.644
$\eta_E = 0.96$	1% η_p	3.79	0.939	0.618

Note: Results are shown for PRO operation at draw and feed inlet crossflow velocities of 14 cm/s and 6 cm/s, respectively, feed outlet crossflow velocity of 0.56 cm/s, ΔP = 18.1 bars, and channel dimensions as listed in Table 2.

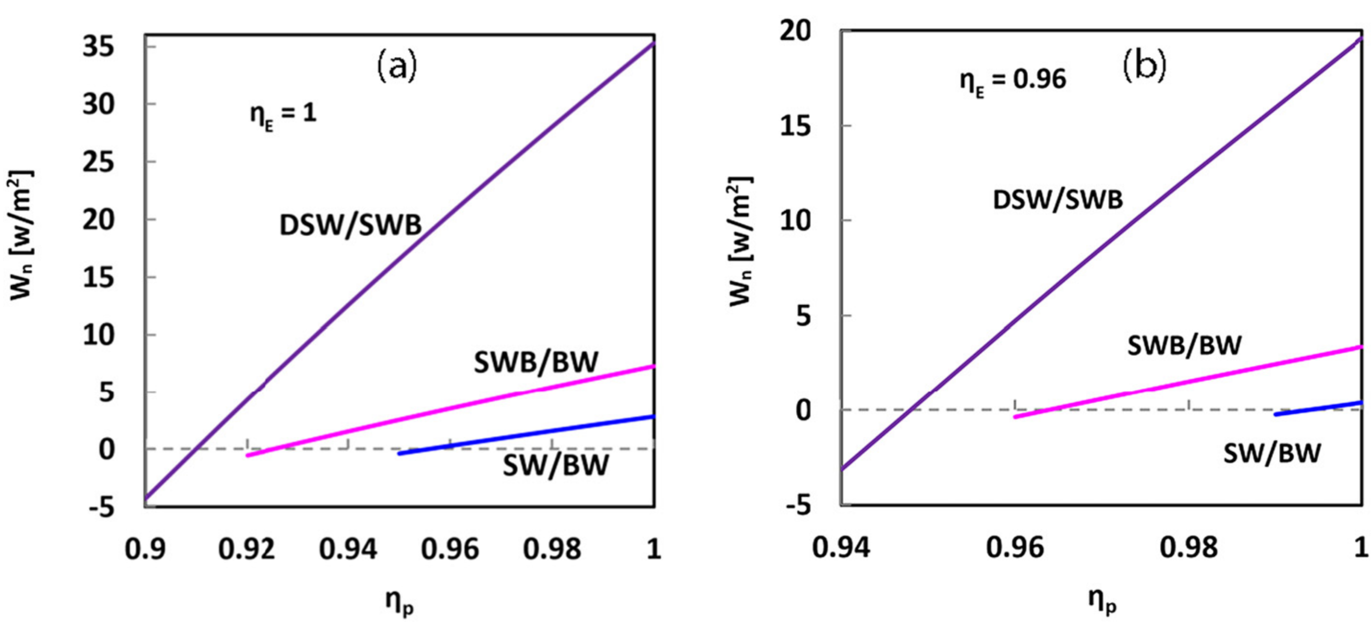

Fig. 9. Variation of net energy production (W_n) with pump efficiency (η_p) for three different draw/feed streams at the high end of pump efficiency (η_p = 0.94–0.96) for the cases of: (a) ideal energy recovery device ($\eta_E = 1$), and (b) for $\eta_E = 0.96$. Draw and feed velocities and channel dimensions were set as in the simulations of Fig. 8. (DSW – Dead Sea water, SW – Seawater, SWB – Seawater RO brine, BW – brackish water).

within the flow channels also increases frictional pressure losses (i.e., greater the pressure drop) which reduces the net extracted energy. As in optimized RO membrane elements, the channel height and stream velocity along the membranes are established so as to minimize pressure losses, and maximize element product water recovery, while also striving to minimize fouling which increases with increased permeate flux. In PRO, the feed stream velocity will decrease along the channel (from inlet to outlet), thereby increasing the importance of CP in this channel (Appendix B) to an extent which is more significant in longer channels than in short laboratory test cells. In contrast, the draw stream velocity increases along the channel (from inlet to exit), given the gain of water from the feed side; thus, frictional pressure losses are expected to increase along the draw channel (Appendix B), while CP will only slightly reduced for the expected Reynolds number increase. The above intricate coupling of hydrodynamics and CP development along the channels calls for optimization of the velocities in both channels to reduce both CP and pressure losses. It is estimated that in 1 m long membrane, the possible tolerance in the extracted energy as per the present analysis is <10%. Since the overall energy gain in the calculated cases presented above (see Section 3.4) is very low and considering a realistic range of pumps and ERD efficiencies, even 20% improvement in the energy balance will not significantly alter the conclusions as portrayed in the analysis leading to the results provided in Figs. 8 and 9.

4. Summary and conclusions

An approach to quantifying the feasible level of osmotic power generation via pressure retarded osmosis (PRO) was developed based on detailed two dimensional finite element (2-D-FEM) PRO model consisting of the fully-coupled hydrodynamics and salt mass transfer equations. The analysis was carried out for a channel length of 1 m which is the typical size expected for commercial size PRO elements. Pressure losses along the feed and draw channels and the efficiencies of pumping and energy recovery were also considered in the analysis. The approach to arriving at the operating conditions that maximize peak power generation was illustrated for the case of PRO membrane of a relatively high permeability. PRO simulations, using experimental membrane transport parameters extracted from experimental data via a 2-D-FEM PRO model, were carried out to determine the required inlet draw and feed inlet velocities that maximize the generated power with illustrative test cases discussed for three different draw/feed stream salinities representing seawater/brackish water (SW/BW), seawater RO-brine/brackish water (SWB/BW), and Dead Sea water/Seawater (DSW/SWB). The analysis revealed that the maximum generated peak power density was highest for DSW/SW (35.3 W/m^2), followed by SWB/BW (7.29 W/m^2) and SW/BW (3.53 W/m^2). Positive net power generation, even for the case of high efficiency (96%), would only be reached if pump efficiencies would be in excess of 99.5%, 96.5% and 94.5%, for PRO with the draw/feed stream pairs of SW/BW, SWB/BW and DSW/SWB, respectively. In assessing the expected performance of PRO for the above cases, it is emphasized that with the selection of optimal draw and feed stream crossflow velocities, the loss (or reduction) in net peak power production is in the ranges of 10–36% caused by reduction in osmotic pressure driving force due to CP, 0.63–1.1% due to frictional pressure losses in the feed, and draw channels and 6–46% due to less than ideal efficiencies (i.e., set as 98%) ERD and pumps. It is noted that with ideal pumps a loss of ERD efficiency of 2%, relative to an ideal ERD, is manifested by 3–23% reduction in the attainable peak power production, as well as about 3–23% loss of net peak power production that would occur for the case of pumps of 98% efficiency but ideal pumps ERD.

Overall, it appears that even for the most optimistic scenario of high PRO energy productivity, from DSW/SW with energy recovery devices and pumps of extremely high efficiencies (96% and 98%, respectively), the maximum peak power density is not likely to exceed ~2 W/m^2 and 12 W/m^2 for the DSW/SWB and SWB/BW PRO cases, while no net positive power generation should be expected for the SW/BW case. It is conceivable that higher permeability PRO membranes could provide somewhat higher performance; however, pressure loses and the need for extremely high efficiency pumps and ERDs would present a significant challenge for PRO as a viable energy generation approach.

Acknowledgements

This research was supported by Grant No. 2014337 from the United States-Israel Binational Science Foundation (BSF). P. The authors also acknowledge support from the California Department of Water Resources.

Appendix A

A.1. Extraction of intrinsic water A and salt B permeability coefficients from PRO data

The intrinsic membrane water permeability (A) and salt transport coefficient (B) were extracted from experimental data channel with spacers as provided in [7]. The average feed and draw stream velocities in the above dataset were calculated, for the data in Fig. 4, PEI 2# membrane of [7], as per the equations of [30] resulting in the velocities provided in Table A1 The CFD PRO model was then utilized to determine the values of A and B by matching model predictions of the water (J_w) and salt (J_s) fluxes with the reported experimental data for these variables. The resulting A and B values in Fig. A1, which were found to vary with the applied transmembrane pressure, were used in the CFD simulations of PRO performance in a long (1 m) channels as described in Section 3.1.

Table A1
PRO Channel parameters for the study of [7] used in the estimation of the cross flow velocities as per the approach provided in [30].

Variable	Draw[(a)]	Feed[(a)]	Equations of [30][(b)]
ε	0.765	0.543	Spacer's porosity, Eqs. (20)–(22)
d_h [mm]	1.31	0.2	Hydraulic diameter, Eqs. (17), (23)
v [cm/s]	11.8	10.4	Cross flow velocity, Eqs. (11), (12)

[a] Spacers SH#2 and SH#3 used in [7] for the draw and feed channels, respectively.
[b] Crossflow velocities and pressure losses in feed and draw channels with spacers were calculated as per the equations in [30].

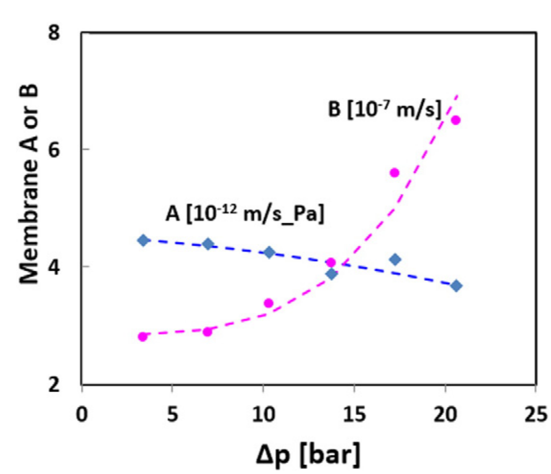

Fig. A1. Dependence of intrinsic membrane permeability coefficients A and B on the hydraulic pressure difference Δp. Dots are of the coefficients derived by the PRO model based on the data in Fig. 4, PEI 2# membrane of [7]. The dashed lines are curves fitted to the extracted A and B values.

Table A2
Information sources utilized for estimation of the pressure loss in the feed and draw channels[(a)].

Channel	Spacers type	Spacers porosity	Spacers thickness [mm]	Hydraulic diameter[(b)]	Friction coefficients[(c)]
Feed (Table A1)	Toray PEC-1000	0.59	0.72	Eqs. (17), (23)	Fig. 7
Draw (Table A1)	Naltex 1228	0.90	0.75	Eqs. (17), (23)	Fig. 6

[a] Pressure losses were calculated using the data and approach provided in [30].
[b] The hydraulic diameter, d_h, was calculated via Eqs. (17), (23) of [30].
[c] Figures of [30] from which friction coefficients were calculated.

A.2. Estimation of pressure losses in the draw and feed channels

Assessment of the net power generation, W_n (Eq. (6), requires determination of the losses in both the feed ($p_{f,loss}$) and draw ($p_{d,loss}$) channels taken to be of 1 m length in the present analysis. Pressure loss in the draw channel ($p_{d,loss}$) was calculated via Eq. (24) of [30] with the parameters reported for the spacer Naltex 1228, Table 11 of [30]. Pressure loss in the feed channel ($p_{f,loss}$) was determined for parameters reported for the Toray PEC-1000, Table A2 and Fig. 7 of [30]. It is noted that the characteristics of the above spacers are similar to those used in [7] which were adopted for the present RO simulations. It is noted that the calculations were accomplished for the equivalent set of spacers that could fit in the channel spacing and that the use of different spacers in the feed and draw channels is common in spiral wound membrane elements [30,38].

Pressure losses were calculated following the approach in [30] whereby the pressure loss is calculated from $P_{loss} = 0.5\lambda\rho V^2 L/d_h$, in which ρ is the solution density, V is the average crossflow velocity and d_h is the hydraulic diameter, i.e., $d_h = 4\varepsilon/(2(b+h)/bh + (1-\varepsilon)S_{v,sp})$ where ε is the porosity of the channel containing the spacers, b and h are feed channel width and height, respectively and $S_{v,sp}$ is the specific spacer surface area. The friction coefficient, λ, for the draw channel is given by $\lambda = 13\,Re^{-0.8}$ and as $\lambda = 6.23\,Re^{-0.3}$ for the feed channel corresponding to the spacer arrangements as per Table A2. Finally, the Reynolds number is defined as $Re = V\cdot d_h/\nu$ in which ν is the kinematic viscosity of the flowing fluid stream.

Table A3
Illustration of power production losses due to frictional losses and pumps and ERD efficiencies for the scenario as in Fig. 9.

PRO operational scenario	PRO power production or loss, W/m^2 (also indicated as % of W_m)		
	DSW/SWB	SWB/BW*	SW/BW
Maximum theoretical power generation, $W_m = A\cdot\Delta\pi^2/4$ (W/m^2)	1039	22.2	9.37
Max power generation considering CP losses, $W_i = J_w\Delta p$ (W/m^2)	36.0 (3.5%)	7.75 (32.9%)	3.98 (42.5%)
Draw side frictional pressure losses, $W_{d,loss}$ (W/m^2)	0.632 (0.061%)	0.42 (1.89%)	0.407 (4.35%)
Feed side frictional pressure losses, $W_{f,loss}$ (W/m^2)	0.043 (0.0041%)	0.037 (0.167%)	0.038 (0.41%)
Power production after accounting for frictional losses $= W_n$ ($\eta_E, \eta_p = 1$) $-$ ($W_{d,loss} + W_{f,loss}$) (W/m^2)	35.3 (3.4%)	7.29 (32.9%)	3.53 (37.7%)
Power production accounting for loss of ER efficiency ($\eta_E = 0.98$) and frictional losses for the case of ideal pumps ($\eta_p = 1$), $W_{n,ER,loss}$ (W/m^2)	22.9 (2.2%)	5.33 (24.0%)	2.39 (25.5%)
Power production accounting for loss of pump efficiency ($\eta_p = 0.98$) and frictional losses for the case of ideal ER ($\eta_E = 1$), $W_{n,pmp,loss}$ (W/m^2)	23.4 (2.25%)	5.44 (24.5%)	2.44 (26.0%)
Net power generation considering frictional losses and 98% and 96% pumping and ERD efficiencies, respectively (i.e., $\eta_E = 0.96, \eta_p = 0.98$), $W_{n,\eta}$ (W/m^2)	10.9 (1.05%)	1.96 (8.83%)	<0

(a) The power production loss are expressed as percentage of the maximum theoretically achievable power density; (b) A and B coefficients were derived via CFD model and experimental data. The coefficients of other two cases were estimated since no data available. (c) Peak power production for the PRO systems of SW/BW, SWB/BW and DSW/SWB was achieved for draw channel inlet pressures of 11.7 bars, 18.1 bars and 117.6 bars, respectively.

Appendix B. Illustration of profiles of solute concentration, osmotic pressure, velocity profiles, water flux and PRO power density

In PRO operation (in the preferred counter-current mode) the osmotic pressure in the draw channel, at the membrane surface, decreases rapidly from inlet toward the exit as the draw stream gains water from the feed side (Fig. B1(a)). At the same time, the osmotic pressure on the feed side, at the support layer skin-side, increases from inlet (i.e., x = 1 m in Fig. B1(b)) toward the feed channel outlet (i.e., x = 0). In the countercurrent configuration there is a severe decline in osmotic pressure in the draw stream inlet region and feed stream outlet regions.

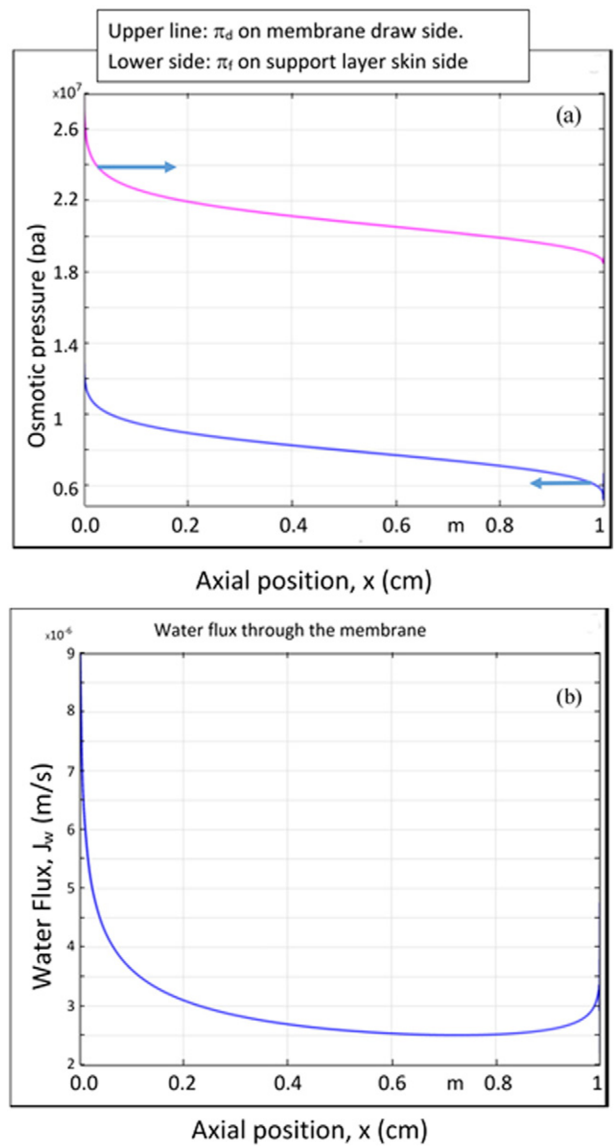

Fig. B1. Simulation results for DSW/SWB PRO operation showing: (top) osmotic pressure at the membrane draw side and support layer skin-side (Fig. 3), and (b) volumetric water flux. Results are Simulations results are for a 1 m long membrane channel with draw and feed channel heights both being 0.71 cm. The inlet draw and feed inlet crossflow velocities were set as 6 and 14 m/s for feed and draw side respectively, as per the scenario of Fig. B4.

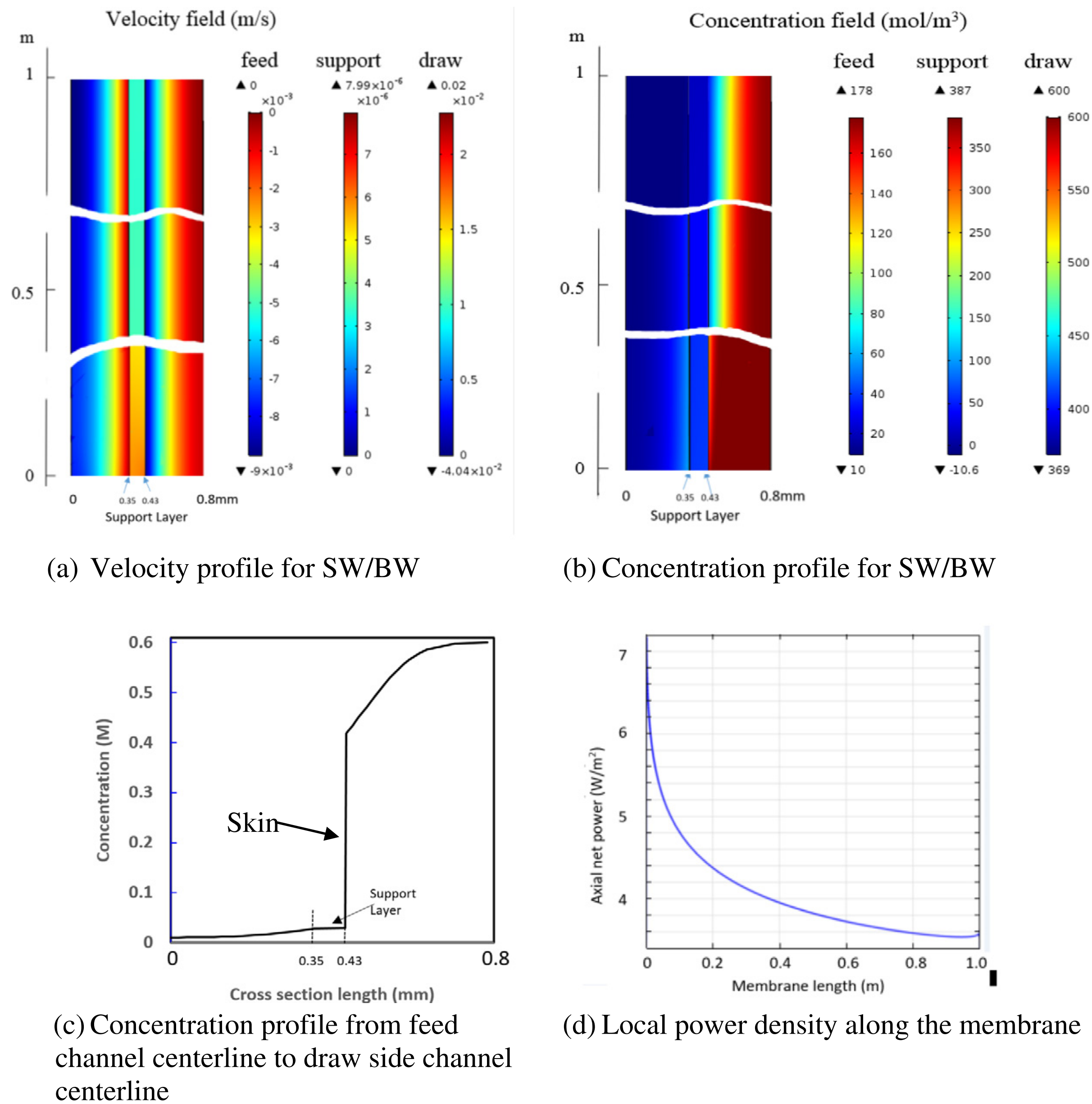

(a) Velocity profile for SW/BW

(b) Concentration profile for SW/BW

(c) Concentration profile from feed channel centerline to draw side channel centerline

(d) Local power density along the membrane

Fig. B2. Illustration of (a) velocity, (b) 2-D salt concentration profile, (c) traverse salt concentration profile (from feed to draw channel across the membrane and support layer, and (d) axial power density profiles. Simulations are for SW (0.6 M)/BW (0.01 M) PRO showing the profiles for channels 1 m long and each (feed and draw) being 0.71 mm in height, with inlet draw and feed crossflow velocities being 14 cm/s and 6 cm/s. respectively and where the peak power density was attained at draw side inlet pressure of 13.7 bars. Note that the support layer domain in the figures is expanded (i.e., it is not to scale) in order to show the profile in this region. In Fig. B2(c) the concentration profile from left to the right is denoted as: feed bulk (x = 0) = 0.0103 M, feed end of the support layer (x = 0.3555 mm) = 0.0279 M; here we note that ECP_f = 0.0176 M, concentration at membrane end of the support layer (x = 0.4315 mm) = 0.0292 M, i.e. ICP = 0.001 M, membrane surface concentration on the draw side (x = 0.431 5 mm) = 0.418 M, and concentration difference across the skin (CDS) i.e. CDS = 0.389 M and ECP_d = 0.182 M. Concentration drop ratio ECP_d/ICP = 182. (Note: ECP_f = concentration difference across the feed-side concentration polarization layer, ICP = concentration difference across the support layer).

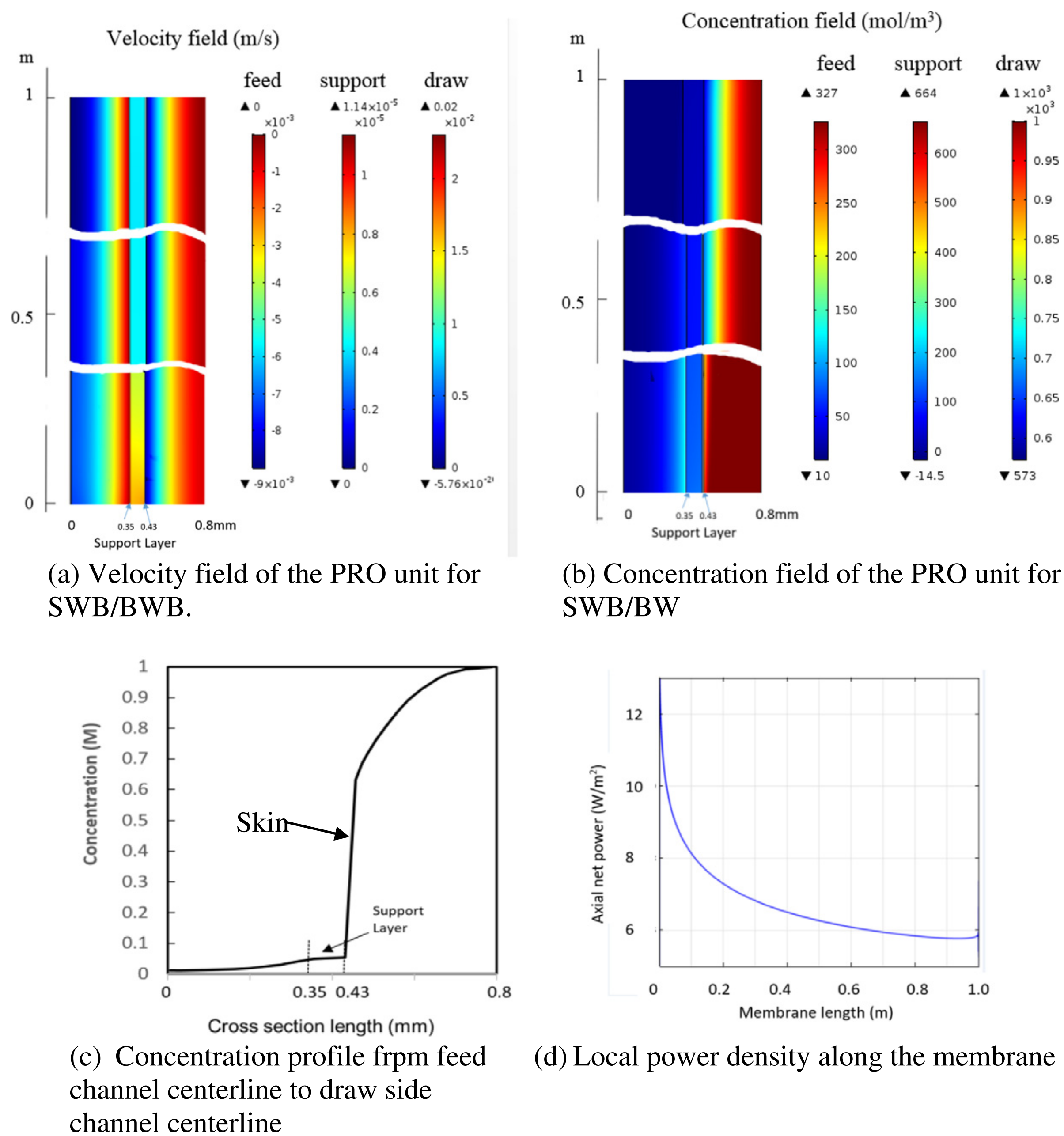

Fig. B3. Illustration of (a) velocity, (b) 2-D salt concentration profile, (c) traverse salt concentration profile (from feed to draw channel across the membrane and support layer, and (d) axial power density profiles. Simulations are for SWB (1 M)/BW (0.01 M) PRO showing the profiles for channels 1 m long and each (feed and draw) being 0.71 mm in height, with inlet draw and feed crossflow velocities being 14 cm/s and 6 cm/s. respectively and where the peak power density was attained at draw side inlet pressure of 13.7 bars. Note that the support layer domain in the figures is expanded (i.e., it is not to scale) in order to show the profile in this region. In Fig. B3(c) the concentration profile from left to the right is denoted as: feed bulk concentration (at x = 0) = 0.0108 M, feed end of the support layer (x = 0.3555 mm) = 0.048 M; here we note that $ECP_f = 0.0372$ M, membrane end of the support layer (x = 0.4315 mm) = 0.054 M, i.e. $ICP = 0.006$ M, membrane surface concentration on the draw side (x = 0.4315 mm) = 0.631 M, and concentration difference across the skin (CDS) i.e. $CDS = 0.577$ M and $ECP_d = 0.423$ M. Concentration drop ratio $ECP_d/ICP = 72$.

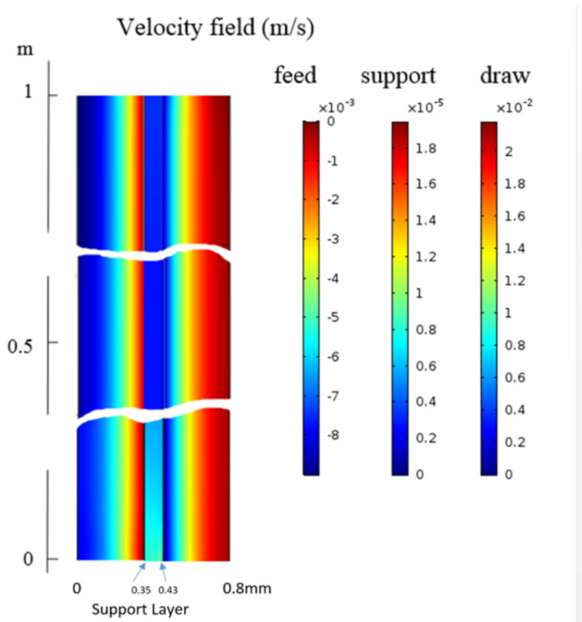

(a) Velocity field of the PRO unit for DSW/SWB

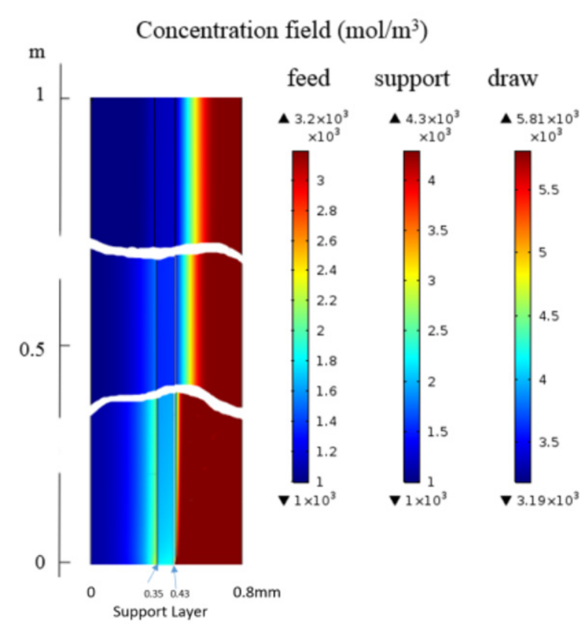

(b) Concentration field of the PRO unit for DSW/SWB

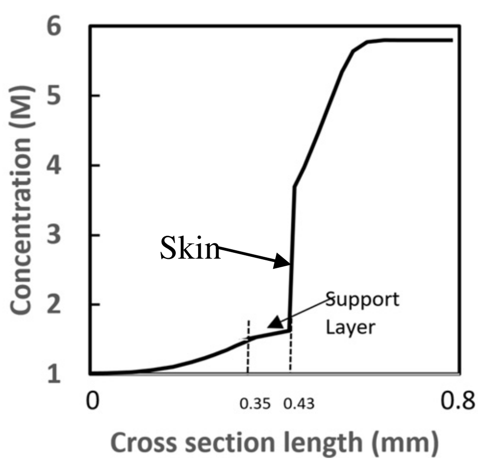

(c) Concentration profile from feed channel centerline to draw side channel centerline

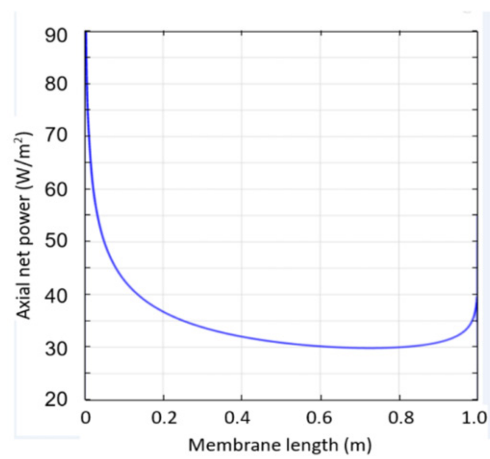

(d) Local power density along the membrane

Fig. B4. Illustration of (a) velocity, (b) 2-D salt concentration profile, (c) traverse salt concentration profile (from feed to draw channel across the membrane and support layer, and (d) axial power density profiles. Simulations are for DSW (5.8 M)/SWB (1 M) PRO showing the profiles for channels 1 m long and each (feed and draw) being 0.71 mm in height, with inlet draw and feed crossflow velocities being 14 cm/s and 6 cm/s. respectively and where the peak power density was attained at draw side inlet pressure of 13.7 bars. Note that the support layer domain in the figures is expanded (i.e., it is not to scale) in order to show the profile in this region. In Fig. B4(c) the concentration profile from left to the right is denoted as: feed bulk (x = 0) = 1.011 M, feed end of the support layer (x = 0.3555 mm) = 1.527 M; here we note that ECP_f = 0.516 M, membrane end of the support layer (x = 0.4315 mm) = 1.624 M, i.e. *ICP* = 0.097 M, membrane surface concentration on the draw side = 3.689 M, and concentration difference across the skin (CDS, x = x = 0.4315 mm), i.e., CDS = 2.065 M and ECP_d = 3.735 M. Concentration drop ratio ECP_d/ICP = 47.3.

Table B3
Density and viscosity of the entering feed and draw solution streams along with the inlet flow rates and Reynolds numbers in the feed and draw channels[(a)].

	ρ [kg/m³]		η [10^{-4} Pa s]		Q [10^{-5} m³/s]		*Re*	
	Feed	Draw	Feed	Draw	Feed	Draw	Feed	Draw
SW/BW	997	1022	8.91	9.41	2.13	4.98	8.94	141
SWB/BW	997	1039	8.91	9.71	2.13	4.98	8.94	139
DSW/SWB	1039	1238	9.71	27.2	2.13	4.98	8.55	59.2

(a) Simulations were carried out for 1 m long channels each being 0.71 mm in height.

References

[1] L. Loeb, Production of energy from concentrated brines by pressure-retarded osmosis, I. preliminary technical and economic correlations, J. Membr. Sci. (1976) 49–63.
[2] F.T. Thorsen, T. Holt, The potential for power production from salinity gradients by pressure retarded osmosis, J. Membr. Sci. 335 (2009) 103–110.
[3] I. Golbeck, X. Li, F. Janssen, T. Brüning, J.W. Nielsen, V. Huess, J. Söderkvist, B. Büchmann, S.M. Siiriä, O.V. Piikkiö, B. Hackett, N.M. Kristensen, H. Engedahl, E. Blockley, A. Sellar, P. Lagemaa, J. Ozer, S. Legrand, P. Ljungemyr, L. Axell, Uncertainty estimation for operational ocean forecast products a multi-model ensemble for the North Sea and the Baltic Sea, Ocean Dyn. 65 (2015) 1603–1631.

[4] Anon, Management Unit of the North sea Mathematical Model (MUMM), (Department VI of the Royal Belgian Institute of Natural Sciences, (2002–2015)).
[5] M. Beyth, The Red Sea and the Mediterranean-Dead Sea canal project, Desalination (2007) 365–371.
[6] M.F. Naguib, J. Maisonneuve, C.B. Laflamme, P. Pillay, Modeling pressure-retarded osmotic power in commercial length membranes, Renew. Energy 76 (2015).
[7] Y. Li, R. Wang, S. Qi, C. Tang, Structural stability and mass transfer properties of pressure retarded osmosis (PRO) membrane under high operating pressures, J. Membr. Sci. 488 (2015) 143–153.
[8] S. Loeb, Production of energy from concentrated brines by pressure-retarded osmosis, II. Experimental results and projected energy costs, J. Membr. Sci. 1 (1976) 249–269.
[9] Q. She, D. Ho, J.K. Liu, H. Tan, C.Y. Tang, Effect of feed spacer induced membrane deformation on the performance of pressure retarded osmosis (PRO): implications for PRO process operation, J. Membr. Sci. 445 (2013) 170–182.
[10] W.A. Phillip, J.S. Yong, M. Elimelech, Reverse draw solute permeation in forward osmosis: modeling and experiments, Environ. Sci. Technol. 44 (2010) 5170–5176.
[11] N.T. Hancock, T.Y. Cath, Solute coupled diffusion in osmotically driven membrane processes, Environ. Sci. Technol. 43 (2009) 6769–6775.
[12] Y.C. Kim, M. Elimelech, Adverse impact of feed channel spacers on the performance of pressure retarded osmosis, Environ. Sci. Technol. 46 (2012) 4673–4681.
[13] S.V.D. Zwan, I.W.M. Pothof, B. Blankert, J.I. Bara, Feasibility of osmotic power from a hydrodynamic analysis at module and plant scale, J. Membr. Sci. 389 (2012) 324–333.
[14] G. Han, S. Zhang, X. Li, T.S. Chung, High performance thin film composite pressure retarded osmosis (PRO) membranes for renewable salinity-gradient energy generation, J. Membr. Sci. 440 (2013) 108–121.
[15] S.S. Hong, W. Ryoo, M.S. Chun, S.O. Lee, G.Y. Chung, Numerical studies on the pressure-retarded osmosis (PRO) system with the spiral wound module for power generation, Desalin. Water Treat. 52 (2014) 6333–6341.
[16] S. Loeb, L. Titelman, E. Korngold, J. Freiman, Effect of porous support fabric on osmosis through a Loeb–Sourirajan type asymmetric membrane, J. Membr. Sci. 129 (1997) 243–249.
[17] N.Y. Yip, A. Tiraferri, W.A. Phillip, J.D. Schiffman, L.A. Hoover, Y.C. Kim, M. Elimelech, Thin-film composite pressure retarded osmosis membranes for sustainable power generation from salinity gradients, Environ. Sci. Technol. 45 (2011) 4360–4369.
[18] C.H. Tan, H.Y. Ng, Modified models to predict flux behavior in forward osmosis in consideration of external and internal concentration polarizations, J. Membr. Sci. 324 (2008) 209–219.
[19] C. Klaysom, T.Y. Cath, T. Depuydt, I.F.J. Vankelecom, Forward and pressure retarded osmosis: potential solutions for global challenges in energy and water supply, Chem. Soc. Rev. 42 (2013) 6959–6989.
[20] N.N. Bui, J.T. Arena, J.R. McCutcheon, Proper accounting of mass transfer resistances in forward osmosis: improving the accuracy of model predictions of structural parameter, J. Membr. Sci. 492 (2015) 289–302.
[21] Y.C. Kima, S. Lee, S.J. Park, Effects of membrane transport properties and structure parameter on pressure-retarded osmosis performance, Desalin. Water Treat. 57 (2016) 10111–10120.
[22] S. Zhao, K. Huang, H. Lin, Impregnated membranes for water purification using forward osmosis, Ind. Eng. Chem. Res. 54 (2015) 12354–12366.
[23] A. Sagiv, A. Zhu, P.D. Christofides, Y. Cohen, R. Semiat, Analysis of forward osmosis desalination via two-dimensional FEM model, J. Membr. Sci. 464 (2014) 161–172.
[24] A. Staub, A. Deshmukh, M. Elimelech, Pressure-retarded osmosis for power generation from salinity gradients: is it viable? Energy Environ. Sci. 492 (2015) 31–48.
[25] A. Sagiv, P.D. Christofides, Y. Cohen, R. Semiat, On the analysis of FO mass transfer resistances via CFD analysis and film theory, J. Membr. Sci. 495 (2015) 198–205.
[26] COMSOL, Multiphysics Software Package, in, 1998–2011.
[27] A.E. Cattaert, High pressure pump efficiency determination from temperature and pressure measurements, IEEE PES Power Africa 2007 Conference and Exposition, Johannesburg, South Africa, 2007 16–20 July.
[28] IDB, Evaluation of water pumping system, Energy Efficiency Assessment Manual, First Edition, 2011 Water and Sanitation Initiative Sustainable Energy and Climate Change Initiative, in, Washington, D.C.
[29] R.L. Stover, Seawater reverse osmosis with isobaric energy recovery devices, Desalination 203 (2007) 168–175.
[30] G. Schock, A. Miquel, Mass transfer and pressure loss in spiral wound modules, Desalination 64 (1987) 339–352.
[31] S. Loeb, Energy production at the Dead Sea by pressure-retarded osmosis: challenge or chimera? Desalination 120 (1998) 247–262.
[32] J. Wei, C. Qiu, C.Y. Tang, R. Wang, A.G. Fane, Synthesis and characterization of flat-sheet thin film composite forward osmosis membranes, J. Membr. Sci. 372 (2011) 292–302.
[33] S. Gunashekar, K.M. Pillai, B.C. Church, N.H. Abu-Zahra, Liquid flow in polyurethane foams for filtration applications: a study on their characterization and permeability estimation, J. Porous. Mater. 22 (2015) 749–759.
[34] S.S. Sablani, M.F.A. Goosen, R. Al-Belushi, V. Gerardos, Influence of spacer thickness on permeate flux in spiral-wound seawater reverse osmosis systems, Desalination 146 (2002) 225–230.
[35] H. Kim, J.S. Choi, S. Lee, Pressure retarded osmosis for energy production: membrane materials and operating conditions, Water Sci. Technol. 65 (2012) 1789–1794.
[36] R. Semiat, Energy demands in desalination processes, Environ. Sci. Technol. 42 (2008) 8193–8201.
[37] T.H. Edvard Sivertsen, W. Thelin, G. Brekke, Pressure retarded osmosis efficiency for different hollow fibre membrane module flow configurations, Desalination 312 (2013) 107–123.
[38] Y.C. Kim, Y. Kim, D. Oh, K.H. Lee, Experimental investigation of a spiral-wound pressure-retarded osmosis membrane module for osmotic power generation, Environ. Sci. Technol. 47 (2013) 2966–2973.